MATERIALS SCIENCE

Enhancement of service life of polymer electrolyte fuel cells through application of nanodispersed ionomer

Chi-Yeong Ahn[1,2]*, Juhee Ahn[3]*, Sun Young Kang[4], Ok-Hee Kim[5], Dong Woog Lee[6], Ji Hyun Lee[6], Jae Goo Shim[6], Chang Hyun Lee[3†], Yong-Hun Cho[4†], Yung-Eun Sung[1,2†]

In polymer electrolyte fuel cells (PEFCs), protons from the anode are transferred to the cathode through the ionomer membrane. By impregnating the ionomer into the electrodes, proton pathways are extended and high proton transfer efficiency can be achieved. Because the impregnated ionomer mechanically binds the catalysts within the electrode, the ionomer is also called a binder. To yield good electrochemical performance, the binder should be homogeneously dispersed in the electrode and maintain stable interfaces with other catalyst components and the membrane. However, conventional binder materials do not have good dispersion properties. In this study, a facile approach based on using a supercritical fluid is introduced to prepare a homogeneous nanoscale dispersion of the binder material in aqueous alcohol. The prepared binder exhibited high dispersion characteristics, crystallinity, and proton conductivity. High performance and durability were confirmed when the binder material was applied to a PEFC cathode electrode.

INTRODUCTION

The electrochemical performance of polymer electrolyte fuel cells (PEFCs) is largely influenced by their key components such as polymer electrolyte membranes, catalysts, and perfluorinated sulfonic acid (PFSA) ionomers (*1*). The redox reactions in a PEFC occur mainly at the electrode interface, called the triple phase boundary (TPB), at which the reactant gases (e.g., H_2 and O_2 at the anode and cathode, respectively), platinum (Pt) catalyst particles on electron-conducting carbon materials, and ionomers come into contact with each other (*2*).

To date, catalysts have been studied primarily in terms of their activity and durability in fuel cells, based on various synthetic methods with calculation results obtained over several decades, with progress having been made compared to conventional Pt-based catalysts (*3*). Unfortunately, the increases in the activity and durability of a factor of ca. 2 to 130, as reported in the literature, were all obtained from liquid-based half-cells, which are suitable for analyzing the characteristics of the catalyst at the laboratory scale. When these catalysts are applied to a membrane-electrode assembly (MEA) for a practical single cell, the performance is much lower than that of a half-cell (*4*). Although the reasons for this phenomenon are unclear, a sufficient number of related studies have not been undertaken, while the performance and durability studies conducted to date have focused only on catalysts or the solid electrolyte membranes themselves.

The ionomer is a factor that greatly affects MEA performance. The performance and durability of a fuel cell can be improved by controlling the characteristics of this ionomer, not the catalyst itself. The ionomer assists with the conduction of the protons within the porous electrodes and acts as a mechanical support for the high–surface area carbon materials on which the nanoscale Pt catalyst particles are distributed (*5*). The impregnation of ionomers for electrode formation contributes notably to the improved electrochemical PEFC performance relative to ionomer-free electrodes (*6*).

PFSA (e.g., Nafion) copolymers are state-of-the-art ionomer materials. PFSA ionomers consist of a chemically robust hydrophobic polytetrafluoroethylene backbone and perfluorinated side chains containing a hydrophilic sulfonic acid ($-SO_3-H^+$) group at each terminal end. Their architectures induce well-defined hydrophobic-hydrophilic microphase-separated morphologies for fast proton conduction (*7*). Furthermore, the high electronegativity of their F atoms enables the easy release of protons from the $-SO_3-H^+$ groups. These ionomers are provided in the form of dispersions in aliphatic alcohol–water mixtures and maintain the inertness of Pt catalysts during electrode formation. Most PEFC systems use Nafion dispersions [e.g., 5 weight % (wt %) Nafion D521, DuPont, USA] because of their high reliability, as demonstrated by accumulated track records. However, Nafion dispersions cannot necessarily offer sufficiently good electrode characteristics to ensure high PEFC performance for long periods.

Several researchers have attempted to overcome this technical issue via chemical and physical routes. Typical synthetic routes adopted by chemical companies are based on the architectural tuning of PFSA side chains. One ionomer modification is the elimination of branched $-CF_3$ groups in the side chains, which induces the tight packing of the PFSA segments and a relatively high level of crystallinity, which is linked to chemical durability (*8*). The chemical resistance of PFSA, particularly to radical degradation, can be improved further through the removal of the swivel ether (—O—) groups from the side chains. Another method grants superacid functionality to the PFSA ionomers by lowering the equivalent weight (ionomer weight per mole of $-SO_3-H^+$ groups, expressed as grams per mole) (*9*) and/or by shortening the side-chain length (*10*). Membrane studies have demonstrated that this methodology is effective in minimizing the reduction in the proton conduction ability in the dry state, but the modified ionomers had reduced mechanical strength under hydrated conditions because of their excessive swelling behavior.

Rather than using chemical routes for membrane applications, most studies of electrode binders have addressed physical routes where

[1]Center for Nanoparticle Research, Institute for Basic Science (IBS), Seoul 08826, Republic of Korea. [2]School of Chemical and Biological Engineering, Seoul National University, Seoul 08826, Republic of Korea. [3]Energy Engineering Department, Dankook University, Cheonan 31116, Republic of Korea. [4]Department of Chemical Engineering, Kangwon National University, Samcheok 25913, Republic of Korea. [5]Department of Science, Republic of Korea Naval Academy, Jinhae-gu, Changwon 51704, Republic of Korea. [6]Creative Future Laboratory, Korea Electric Power Corporation Research Institute, Daejeon 34056, Republic of Korea.
*These authors contributed equally to this work.
†Corresponding author. Email: chlee@dankook.ac.kr (C.H.L.); yhun00@gmail.com (Y.-H.C.); ysung@snu.ac.kr (Y.-E.S.)

ionomer dispersion characteristics such as average colloidal particle sizes and shapes, and impregnation contents are controlled by varying the solvent ingredients (*11*,*12*) and/or compositions (*13*,*14*). The dispersion characteristics seem to determine the electrochemical activity of the TPB, particularly in the cathode. For example, when colloidal PFSA particles are smaller than the diameter (ca. 20 to 40 nm) of the primary pores, defined as the space within the catalyst agglomerates, they are easily located in the pores and improve the catalyst utilization (*15*). Meanwhile, ionomers with colloidal sizes greater than 40 nm can penetrate the space (i.e., secondary pore) between the catalyst agglomerates and affect the mechanical stability of the electrode layers.

Here, we describe an ionomer dispersion with an average colloidal particle size much smaller than that in commercially available dispersions, obtained by treating a Nafion 117 membrane with aqueous aliphatic alcohol under supercritical conditions. Supercritical fluids (SCFs) are widely used in industry and research because of their unique properties (*16*). They are particularly useful in the synthesis of special medicines (*17*), polymers (*18*), and nanomaterials (*19*) that are difficult or impossible to obtain under typical conditions; they have also been investigated to prepare materials for electrochemical applications (*20*). To date, however, the efficacy of the superacidic PFSA ionomers as electrode binders has not been revealed. To improve the dispersion characteristics of a conventional ionomer, SCF conditions were used in our study. Above their critical points, SCFs have high solvation power, negligible surface tension similar to those of liquids, and transport properties similar to those of gases. The density values of SCFs enable substantial solvation power; they show high solute diffusivity (in this case, PFSA ionomers) because the solute viscosity is lower in SCFs, thus facilitating mass transfer (*21*–*23*). Their solubility for specific solutes can be further improved by incorporating co-solvents. Here, we used supercritical isopropyl alcohol (IPA) together with water as a polar miscible co-solvent to enhance the polarity and solvation strength of the SCF via the formation of hydrogen bonds. Also, the fundamental characteristics of the resulting ionomer dispersion were compared with those of chemically identical Nafion D521. Last, the electrochemical availability of the SCF-treated ionomer as a cathode binder was evaluated under both practical PEFC operation conditions and harsh electrode acceleration conditions. Schematic diagrams of conventional and SCF-treated ionomers on the catalyst surfaces are shown in Fig. 1.

RESULTS

The laboratory-made ionomer dispersion was obtained by treating a Nafion membrane in an aqueous medium containing IPA [T_c = 239°C and P_c = 7.89 MPa (*24*)] in the SCF state. Nafion 117 was chosen as the starting material because of its relatively low cost by mass compared to other solid-state Nafion materials of different configurations such as membranes, resins, pellets, or powders. However, a Nafion 117 membrane is not the only feasible material for laboratory-made dispersions and could be replaced with another material considering the cost efficiency and material characteristics.

Fundamental characteristics of synthesized ionomer dispersion

The supercritical dispersion was transparent, like Nafion D521. Dynamic light scattering (DLS) analysis showed that both dispersions exhibit trimodal ionomer particle distributions (Fig. 2A). However, the size characteristics of the ionomer particles in the laboratory-made dispersion differed largely from those in D521. Most D521 particles (ca. 94%) were larger than 100 nm, while the remainder (ca. 6%) were dispersed in the nanoscale region (*Z*-average diameter = 267.2 nm). Meanwhile, the laboratory-made dispersion contained many ionomer particles with sizes smaller than 100 nm (*Z*-average diameter = 9.4 nm). The number of particles smaller than 100 nm was up to seven times greater than in the case of D521. Even the ionomers in the largest-size region (59%) did not exceed 1.7 μm; the greatest concentration of these particles was located at ca. 255 nm. This was due to the solubility of the ionomer in the alcohol-based solvent increasing under supercritical conditions, which lessens the entanglement of the polymer chains. Then, upon cooling to a temperature below the critical point, the separated polymer chains appear to become independently entangled, resulting in their rearrangement into smaller particles. Therefore, the laboratory-made dispersion is henceforth defined as a nanodispersion (ND).

Viscosity analysis was helpful in understanding the fundamental properties of the ND. The 5 wt % ND exhibited a viscosity that was four times greater than that of the D521 dispersion of an identical concentration, regardless of the applied shear rate (Fig. 2B). This was attributed to the relatively small size of the ionomer particles. In general, the overall surface areas of the ionomer particles increase as their sizes decrease. Thus, dispersed nanosized ionomer particles are expected to experience stronger secondary interactions (e.g., hydrogen bonding, dipole-dipole interaction, and/or London dispersion forces) between ionomer particles or between the ionomer particles and solvent molecules, compared to dispersed microsized particles. This is likely responsible for the high viscosity of the ND. In addition to the ionomer particle size, another important factor in determining the viscosity is the ionomer molecular weight. Gel permeation chromatography (GPC) measurements showed that the ND had a much higher number average molecular weight (M_n) and weight average molecular weight (M_w) than D521, as summarized in Table 1. These molecular weight differences likely arise from the different synthetic routes. D521 was synthesized directly via the expensive aqueous emulsion copolymerization of the monomers of perfluorosulfonyl fluoride ethylpropylvinyl ether (PSEPVE) and tetrafluoroethylene (TPE), without emulsifiers (e.g., ammonium perfluorooctanoate) (*25*). Conventional emulsion polymerization promotes narrow molecular weight distributions (MWDs), expressed in terms of the polydispersity index (PDI = M_w/M_n). However, the emulsifier-free reaction atmosphere created a relatively broad MWD for D521 with a PDI of ca. 3. The ND was easily prepared with solid-state Nafion membranes polymerized from PSEPVE and TPE through a free-radical mechanism in perfluorocarbon solvents containing a perfluorinated initiator (e.g., perfluoroperoxide derivative) (*26*,*27*). The PDI value of ca. 1.5 was comparable to those of well-controlled chain-growth polymers with a very narrow MWD (*28*). The plot of the viscosity values of the ND versus applied shear rate in Fig. 2B shows that the former were independent of the shear rates, which indicates that the ND had high dispersion stability, analogous to that of D521.

The ND experienced a phase transition from an aqueous dispersion to a solid when it was used as a cathode binder, which necessitated the characterization of the solid-state ionomer. The ionomer density comparison in the dry membrane state (Table 1) indicated that small ionomer particles assisted in the dense structural formation by reducing the free volume during solidification. The crystallinities of D521 and ND were obtained from x-ray diffraction (XRD) analysis. This feature can be quantitatively analyzed by deconvoluting each

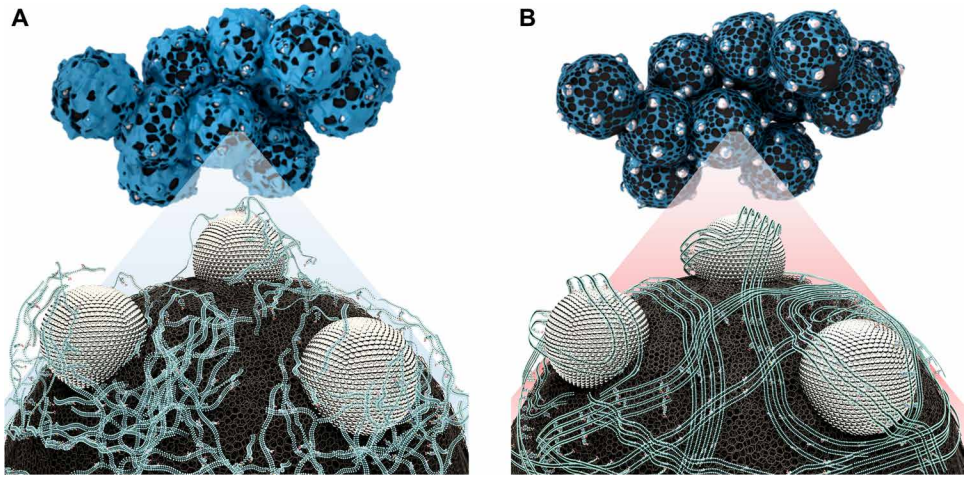

Fig. 1. Schematics of Nafion ionomers on the catalyst surfaces. (**A**) Distribution of conventional ionomers synthesized by emulsion polymerization. (**B**) Distribution of the laboratory-made ionomers synthesized by SCF process. Enlarged conceptual diagram showing the distribution of both conventional and prepared ionomer on the Pt/C catalyst surface. The SCF process contributes to the formation of nanodispersed Nafion ionomer, leading to improved electrochemical performance and durability.

XRD peak as individual amorphous (green line) and crystalline (blue line) peaks with the following Gaussian equations

$$\text{Crystallinity}\,(x_c) = \frac{\int_0^{\infty} I_c(q)\, q^2\, dq}{\int_0^{\infty} [I_c(q)\, q^2 + I_a(q)\, q^2]\, dq} \quad (1)$$

$$\text{Diffraction vector}\,(q) = \frac{4\pi}{\lambda \sin(\theta/2)} \quad (2)$$

where λ and θ are the wavelength of the Cu Kα x-ray source and the diffraction angle, respectively, and $I_c(q)$ and $I_a(q)$ indicate the sums of the fitted crystalline and amorphous peak intensities, respectively. The XRD peak of the ND (Fig. 2D) was sharper than that of D521 (Fig. 2C), indicating that the semicrystalline ND chains were packed with relative uniformity and improved regularity. The crystalline content (41.8%) of the ND was much higher than 25.8% of D521, despite the chemical architecture and equivalent weight being identical. Even if they have the same chemical structure, the entanglement properties of the polymer chains are very important for determining the crystallinity of the polymer. Also, even if the molecular weight is relatively low, the particle size may become large if the polymer chains are entangled at the microlevel. On the other hand, in the same way as with ND, even if the molecular weight is high, when the particles are entangled at the nanolevel, they become tightly solidified, which increases the density of the polymer. Further, at the same time, self-assembly between the hydrophilic and hydrophobic functional groups improves the regularity of the polymer packing, thereby increasing the crystallinity. In general, improved crystallinity in a semicrystalline copolymer positively affects its mechanical toughness and chemical resistance (*29*, *30*). Therefore, the mechanical strengths of the ionomers were measured and the results are shown in Table 2. However, the mechanical strengths of the D521 and ND ionomers are too low to be measured as specified in ASTM D882 with a mechanical testing machine (INSTRON 1708, Boston, MA, USA) when thermally treated at low temperatures, which are chosen to minimize the negative thermal impacts such as catalyst sintering during cathode formation. Thermal treatment at 140°C enables mechanical distinction: the D521 ionomer could not be mechanically evaluated because it is extremely brittle, while the ND ionomer exhibited a tensile strength and elongation comparable to that of the D521 ionomer thermally treated at 220°C, which is commonly used for membrane fabrication. The improved mechanical strength of the ND ionomer may arise from a synergistic effect of the high molecular weight and improved crystallinity. Therefore, it can be predicted that the stability of the MEA increases when this ionomer (binder) is introduced into the electrode. This result will be discussed in the next durability section of the MEA.

Table 1. Basic characteristics of D521 and ND in dispersed and membrane states.

	Unit	D521	ND
M_n*	(kDa)	66	95
M_w*	(kDa)	193.7	293.5
PDI*	(–)	2.93	2.15
Density†	(g cm^{-3})	1.93	2.32
Water uptake†	(%)	35.2	26.7
Crystallinity†	(%)	25.8	41.8

*GPC measurement using an *N*-methyl-2-pyrrolidinone (NMP) column. Each ionomer sample was dissolved in NMP containing 0.05 M LiCl. †Before the measurements, each ionomer dispersion was converted to membrane coupons after thermally drying at 60°C for 8 hours and 140°C for 1 hour.

The inter- and intra-molecular arrangements of the ionomer chains constituting hydrophilic and hydrophobic moieties can affect the morphological ordering associated with ion transport channel formation. Typical PFSA ionomer morphologies feature hydrophilic domains that are homogeneously distributed within the hydrophobic matrices. Figure 2E shows the small-angle x-ray scattering (SAXS) spectra measured at an irradiation angle of 90°. All the Nafion ionomers exhibited strong scattering maxima, attributed to the ionic aggregation of the hydrophilic moieties, regardless of the dispersion. The width of the characteristic peak of the ND was smaller than that of D521, indicating that the average size of the hydrophilic domains in the ND was relatively small. As described above, the hydrophilic/hydrophobic

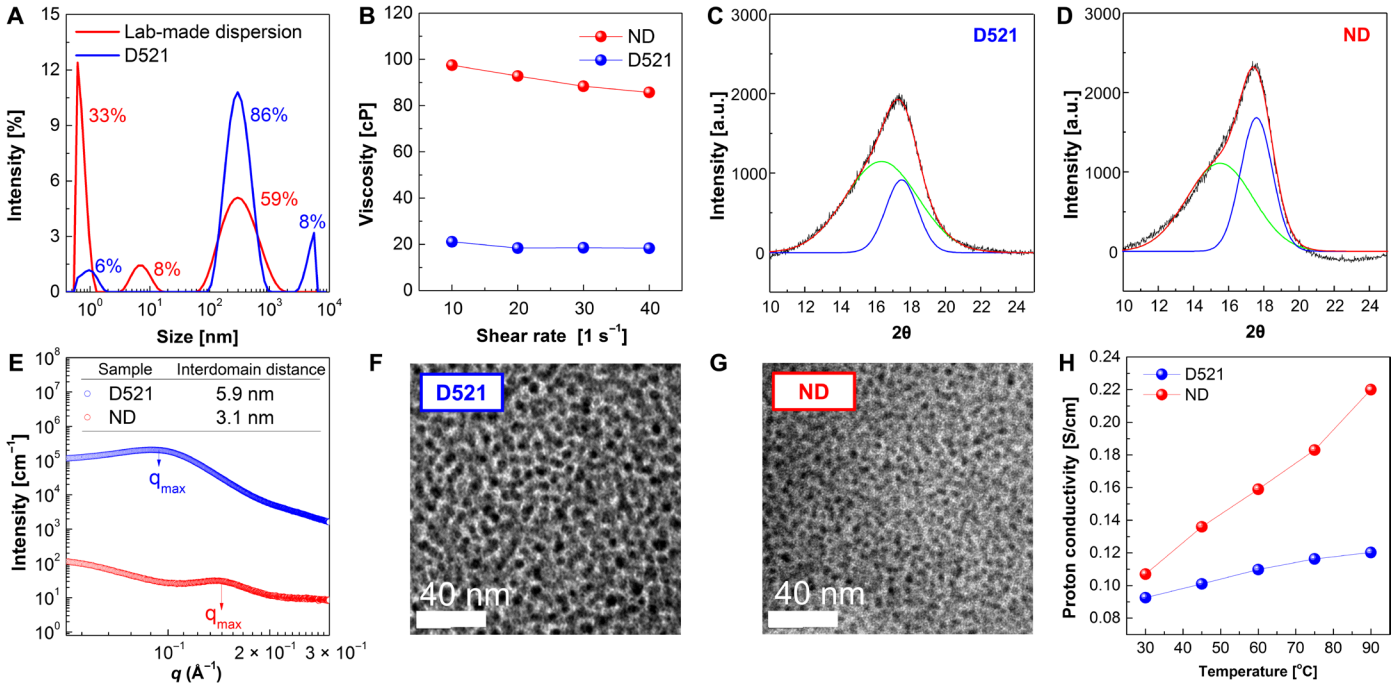

Fig. 2. Physical properties of solidified-state ionomers. (**A**) Particle size distribution pattern by DLS. Most D521 particles are in the ~100-nm range, but the laboratory-made dispersion has a large amount of particles in the nanoscale region. (**B**) Viscosity behaviors of D521 and ND. Because of the relatively small ionomer particle sizes, ND shows four times the viscosity of D521. (**C** and **D**) XRD patterns of solid-state D521 and ND. The sharp XRD peak of ND ionomer indicates that semicrystalline ND ionomer chains are relatively uniformly packed with improved regularity. This feature is quantitatively analyzed by deconvoluting each XRD peak as individual amorphous (green line) and crystalline (blue line) peaks with Gaussian equations. (**E**) SAXS spectra of solid-state D521 and ND. The narrow width of the SAXS peak of ND indicates the relatively small average size of its hydrophilic domains. TEM images of (**F**) D521 and (**G**) ND to compare the size difference of hydrophilic domains (dark regions). (**H**) Proton conductivities of D521 and ND membrane coupons obtained in deionized water as a function of temperatures. Each coupon was thermally treated at 140°C for 1 hour. a.u., arbitrary units.

Table 2. Mechanical strengths of D521 and ND ionomers after thermal treatment.

	Thermal treatment temperature*	Tensile strength	Elongation
	(°C)	(MPa)	(%)
ND	60	8.7	60.9
	120	13.5	68.5
	140	23.1	180.8
D521	140	–†	–†
	220	19.5	199.1

*All thermal treatments were performed in a vacuum oven under N_2 atmosphere for 1 hour. †Not applicable.

domains were influenced by the rearrangement of the polymer chains and the difference in the entanglement characteristics. The size difference in the hydrophilic domains (dark regions) was visually confirmed in transmission electron microscopy (TEM) images, shown in Fig. 2 (F and G). The single q_{max} scattering peak, derived from the ND, was positioned in a higher q vector direction (Fig. 2E) than that of the corresponding q_{max} peak of D521. This variance becomes more distinct when each q_{max} value is converted using Bragg's law to the interdomain distance, which is the average distance between the hydrophilic domains of the ionomer. The interdomain distance of the ND was approximately one-half of that of D521, which is well matched with the TEM images (Fig. 2, F and G). Figure 2H shows the proton conduction capabilities of the solidified ionomers. The ND exhibited faster proton transport behavior than D521. Their differences increased at the elevated temperatures. This was likely due to the shortened proton transport pathway formed between the hydrophilic domains via effective spatial arrangement derived from the ND ionomer particles. The improved proton conductivity of the ND implies a lower resistance such that a high level of performance of the MEA can be predicted for single-cell operation.

Characterization of the catalyst layer

The prepared ionomer dispersion using SCF showed better properties, as mentioned above, than conventional D521, but its characteristics should also be improved when the ionomer is applied to an electrode with a catalyst such as Pt/C. Scanning electron microscopy (SEM) and mercury intrusion porosimetry (MIP) were conducted to analyze the catalyst layer properties after the preparation of MEAs using the same amount (30 wt %) of D521 and ND ionomers. The results are shown in Fig. 3. When observed at low magnification, large white lumps corresponding to bulky ionomer aggregates are observed on the surface of the MEA with D521 (Fig. 3A), but a relatively uniform surface is observed on the surface of the MEA with ND (Fig. 3D). White lumps are also observed in Fig. 3D, but they are much smaller and more uniform in size than the lumps in Fig. 3A. This is because the ND ionomer is well dispersed on the surface of the Pt/C catalyst in the ink slurry for the preparation of the MEA; it maintains its

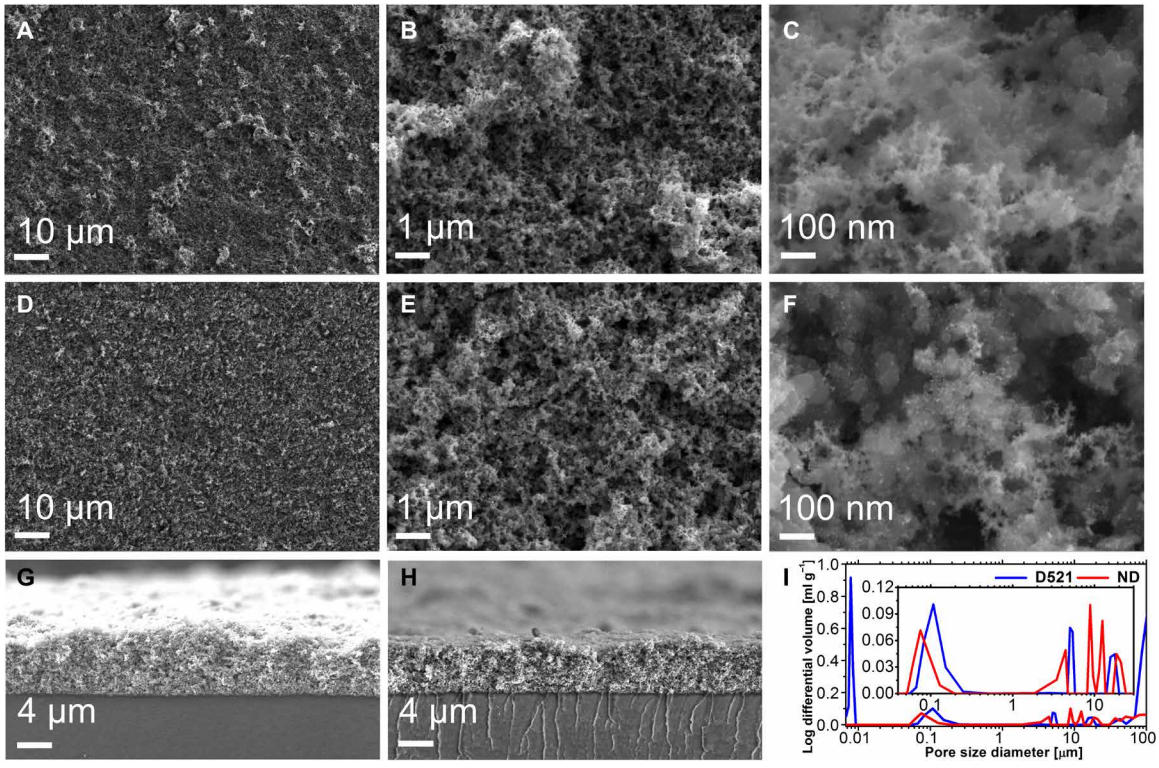

Fig. 3. Surface morphologies and pore distributions of MEAs with conventional D521 ionomer and ND ionomer. SEM results of (**A** to **C** and **G**) MEA with conventional D521 ionomer and (**D** to **F** and **H**) MEA with ND ionomer. (**I**) MIP results of MEA with conventional D521 ionomer (blue) and ND ionomer (red). The inset is an enlarged graph showing the pore distribution near 0.1 to 10 μm.

dispersed state during the drying of the IPA/water solvent, unlike D521. When observing the surface of the MEA at ×10,000 magnification (Fig. 3, B and E), it is confirmed that secondary pores are developed in the catalyst layer in both cases. However, bulky ionomer aggregates are found in the upper left and lower right in Fig. 3B, indicating that some aggregates are in the form of large dendrites. On the other hand, in the case of the MEA with ND, no large aggregated white lumps (ionomer aggregates) are found; the ionomers are dispersed evenly inside the catalyst layer. At ×100,000 magnification (Fig. 3, C and F), the SEM results show that the ionomer covers the surface of the catalyst layer as dendrites in both cases. Further, it is confirmed that the bare Pt nanoparticles (white dots) are exposed because the ionomer does not completely cover the catalyst layer to form an appropriate triple-phase boundary (as described later). The biggest difference is the size of the ionomer aggregates. The D521 ionomer (Fig. 3C) covers the catalyst layer as large lumps, as expected. Moreover, the cross-sections were observed by SEM to confirm the degree of packing of the catalyst layer. The average catalyst layer thicknesses of MEAs with D521 and ND ionomers were found to be 6.71 and 5.76 μm, respectively. Despite the application of the same amount of Pt/C catalyst and ionomer, the catalyst layer in the MEA with D521 was about 16% thicker. MIP analysis was conducted to obtain additional information on the packing of the catalyst layers, as shown in Fig. 3I. MIP was used to analyze the pore structure of the catalyst layers because secondary pores are difficult to characterize using gas adsorption/desorption, such as the Brunauer-Emmett-Teller technique. The porosities measured by MIP were 74.54% and 47.41% in MEAs with D521 and ND, respectively. This agrees with the thicker catalyst layer of MEA with D521 relative to that of MEA with ND. In addition, MEA with D521 exhibits a large primary pore distribution below 10 nm and a relatively undeveloped secondary pore structure. However, for MEA with ND, the colloidal PFSA particles are small and easily located in the primary pores inside the catalyst; therefore, pores of 10 nm are rare. Secondary pores are well developed compared to those in the D521 layer. In the case of MEA with D521, large pores are observed at around 100 μm, attributed to the large ionomer aggregates observed by SEM. On the basis of the morphologies and pore size distribution of the catalyst layer, it is found that the ND has a better ionomer dispersibility for fuel cell use in the MEA.

Effect of ionomer (binder) loading in electrode

The binder content is important in electrode formulation because it is one of the components that determine the TPB. The ionomer ratio in the electrodes must be tuned whenever one of the electrode components is changed. Excessive ionomer impregnation may prevent the reactant gases from reaching the TPB by reducing the gas flux, while low ionomer contents are less desirable in providing effective proton transport pathways in the electrode layers (*31*).

According to a previous report (*32*), D521 exhibited good performance when 30 wt % of the content was loaded in the electrode. For comparison, the electrochemical performances of MEAs using cathodes with 30 wt % D521 (MEA-0) and 10, 20, and 30 wt % ND (MEA-10, MEA-20, and MEA-30) (fig. S1A) were measured. In the low–current density region, their performances increased with the ionomer contents. The maximum power density of the single cells also increased in the same way. Because the ionomer provides proton

transfer pathways, the amount of ionomer could affect the performance of a single cell in the low–current density region. However, in the high–current density region (above 3000 mA cm^{-2}), the performance of the MEA-30 decreased. This is because of mass transport issues observed in the high–current density region, where water was produced as a result of electrochemical reactions at the cathode. In addition, multiple studies (*33*,*34*) have found that heavy ionomer loading in the electrode hinders TPB formation and gas reactions. Therefore, an appropriate amount of ionomer is necessary for MEA fabrication; in our case, MEA-20 exhibited the highest performance among all the MEAs in an O_2 atmosphere. Its performance was better than that of MEA-0, even though it had a lower ionomer content. The electrochemical performances of MEAs (fig. S1B) were also measured in air. Irrespective of the MEA, fuel cell performances decreased severely in air because of inert N_2 reducing the O_2 concentration. However, the use of air is advantageous in terms of its abundance and accessibility. Similar to the O_2 condition, a high ionomer loading led to an improved voltage value in the low–current density region. Meanwhile, the single-cell performance of MEA-10 with the lowest ionomer content was the highest in the high–current density region, where generated water molecules caused the mass transport limitation. Water molecules were easier to discharge when the supply flow rate was five times higher to compensate for the lower O_2 concentration in air. This phenomenon is particularly noticeable when the ionomer content is low (*35*). For an identical content, the current density in the cathode using the ND ionomer was 1.2% (11 mA cm^{-2}) higher at 0.6 V than when using D521. Meanwhile, when 20 wt % of ND was used, the performance gap was widened by 4.6% to 41 mA cm^{-2}. This is because the high proton conductivity obtained through the SCF treatment of the ND leads to the high performance of the MEA even when present in smaller amounts than D521. (Detailed current densities and power densities are given in table S1.)

Single-cell performance and the AST

MEA-20 and MEA-0 were chosen as accelerated stress test (AST) samples to evaluate the electrochemical durability over a short period. In particular, AST was performed to see how the application of different ionomers to each cathode affects the PEFC durability. AST was carried out by a load-cycling method, which causes severe degradation of the cathode electrode (*36*). AST induced electrochemical damage on all the MEAs used in the present study. However, the degree of electrochemical degradation was highly dependent on the type of ionomer used in the cathode. With O_2 (fig. S2, A and B), the performance of MEA-0 at 0.6 V was reduced by 20.0%, while MEA-20 maintained its electrochemical performance within 3.33%. A similar trend was observed in air (Fig. 4, A and B); the current density of MEA-20 at 0.6 V fell by 3.19% (30 mA cm^{-2}), but while that of MEA-0 did by 18.9% (170 mA cm^{-2}) after AST. The electrochemical durability of MEA-20 was about six times higher than that of MEA-0 in terms of the current density. Even after the AST, the current density of MEA-20 at 0.6 V (909 mA cm^{-2}) remained higher than the initial current density of MEA-0 (898 mA cm^{-2}). In addition, low voltages were observed from the low–current density region in MEA-0, while the voltages remained in MEA-20 up to ca. 800 mA cm^{-2} after AST. This decrease in the performance in the low-current region is referred to as the activation loss, which is mainly related to the degradation of the catalyst. Therefore, it was predicted that the degradation of the catalyst was serious in MEA-0 but was barely noticeable in MEA-20. The improved electrochemical tolerance in the ND electrode (MEA-20) was likely associated with the significantly enhanced mechanical toughness derived from the high molecular weight and improved crystallinity of the ionomer. This implies that the improved properties of the ND help prevent catalyst degradation. (The detailed current densities and power densities before and after AST are given in table S2.) In the high–current density region, both MEAs suffered performance degradation. This is probably due to the gradual degradation of secondary pores related to mass transfer under the harsh electrochemical conditions of AST. Electrochemical impedance spectroscopy (EIS) measurements were conducted under both O_2 (fig. S2) and air (Fig. 4, C and D) to monitor the changes in the electrochemical resistance according to AST. Under O_2, the charge-transfer resistance (R_{ct}) of MEA-0 increased from 0.075 to 0.095 ohm·cm^2 (26.7% increment), but that of MEA-20 changed only slightly, even after AST (fig. S2). Further, the semicircular Nyquist plots of MEA-0 and MEA-20 under air are shown in Fig. 4 (C and D). The diameter of the plot for MEA-0 was bigger than that of MEA-20 irrespective of AST. While the R_{ct} value of MEA-0 increased by 39.9% (139 ohm·cm^2), the increment in R_{ct} of MEA-20 was only 32 ohm·cm^2. These distinctive EIS results were well matched with their single-cell performance trends. This indicated that the narrowed proton transport pathway between the hydrophilic domains (Fig. 2G) was the primary contributor to lowering the ohmic resistance in MEAs constituting the same components except for the cathode ionomer materials. After AST, the ND electrode performance was reduced by only 3.19%, but the D521 electrode performance was decreased by 18.9% (under air), together with a large increase in the resistance (the detailed EIS results before and after AST are given in table S3). Also, the ionomer species does not seem to affect the ohmic resistance (R_{ohm}) of the initial fuel cell performance. However, as the AST progresses, the difference in R_{ohm} between the two MEAs becomes large. This demonstrates that the ND ionomer significantly impedes R_{ohm} increase in the MEA because of the improved physical properties. Cyclic voltammetry (CV) analyses were conducted to confirm the change in the electrochemically active surface area (EAS) before and after AST, with the results shown in fig. S4. The results are presented in terms of current density versus voltage for a normal hydrogen electrode. MEA-20 exhibited a slightly higher initial EAS (41.86 m^2 s^{-1}) than MEA-0 (40.93 m^2 s^{-1}). This could be attributed to the hand spraying of the catalyst inks, although the amount of catalyst loading was controlled. After AST, the EAS of MEA-0 was greatly reduced to 26.34 m^2 s^{-1} (a 35.6% decrement), but a loss of only 24.0% was observed for MEA-20. Moreover, because the durability is highly sensitive to ionomer content, the ASTs of MEA-30 and MEA with 20 wt % of commercial D521 ionomer were also conducted to confirm the dependence on ionomer content (fig. S3). Despite containing the same amount of ND ionomer as MEA-0, the performance decrease of MEA-30 (fig. S3A) (0.99% decrement in current density at 0.6 V and 5.56% decrement in maximum power density, as shown in fig. S3C) after AST was smaller than that shown by MEA-0 (18.9% decrement in current density at 0.6 V and 17.8% decrement in maximum power density). In addition, the initial performance of MEA-30 was slightly lower than that of MEA-20, as shown in fig. S1, but the performance decrease after AST was lower than that of MEA-20. This directly demonstrates that the durability of the MEA in the fuel cell is affected by the ionomer content. However, because both the durability and electrochemical performance are important, the optimal ionomer content must be identified to manufacture the MEA. Furthermore, the MEA with the same amount of commercial D521 ionomer (20 wt %)

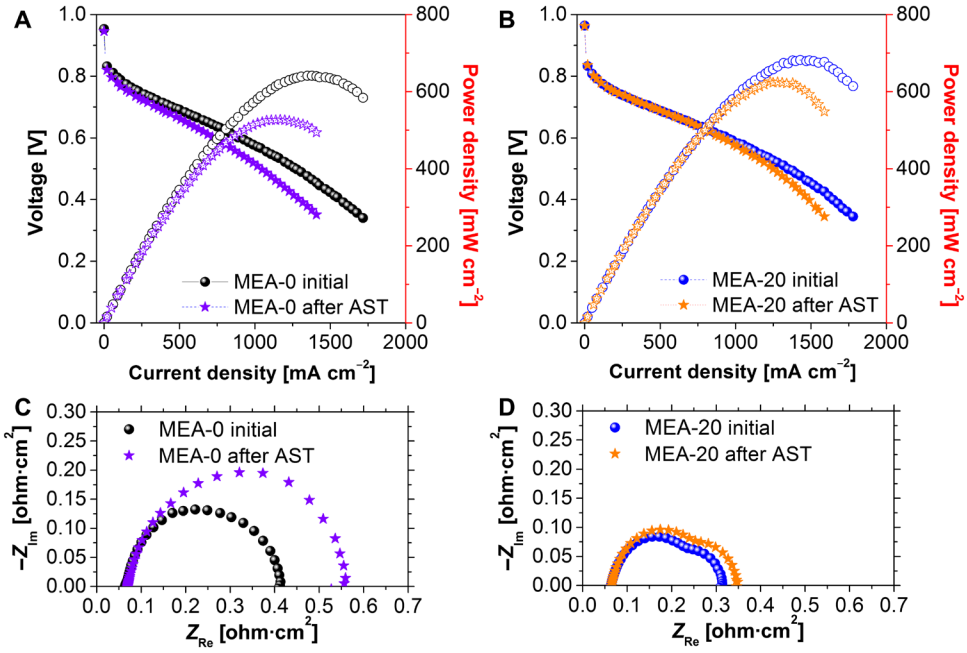

Fig. 4. Polarization curves and EIS results of MEAs with conventional D521 ionomer and ND ionomer before and after AST. Fuel cell performances of MEAs before and after AST. (**A**) MEA with conventional D521 ionomer. (**B**) MEA with ND ionomer in air. EIS results for MEAs before and after AST. (**C**) MEA with conventional D521 ionomer. (**D**) MEA with ND ionomer in air.

showed a greater performance decrease after AST (fig. S3B) than MEA-20. The tendency of performance decrease was similar to that of MEA-0, which is attributed to the weak crystallinity of D521. Therefore, when the same amount of ionomer was applied, high durability was confirmed in the ionomer with applied ND after AST.

TEM analysis was performed to confirm the physical changes in the electrodes after AST (fig. S5); less catalyst degradation occurred in the ND electrode. The initial Pt particles have an average size of 3.49 nm. After AST, the particle size is approximately doubled (6.93 nm) in the D521-applied electrode, but increased by only ca. 0.5 nm (3.94 nm) in the ND-applied electrode. It was determined that the extremely enhanced electrochemical durability was derived from improved mechanical strength. In addition to high molecular weight, the improved crystalline characteristics of the ND contributed to the improvement of mechanical strength, which is believed to primarily influence its electrochemical durability over extended periods, because the tough ionomer binder was more difficult to be washed out during PEFC operation.

DISCUSSION

Here, we have demonstrated the preparation and characterization of an ND ionomer with an average particle size that is smaller than that of a D521 ionomer with an identical chemical architecture and equivalent weight. Furthermore, the electrochemical efficacy of ND as a cathode binder material was also confirmed. The ND ionomer obtained via the SCF process showed unique SAXS and TEM morphologies in which small hydrophilic domains were homogeneously distributed with shortened interdomain distances in the matrices. These morphologies correspond to improved proton conductivity and single cell performances, which resulted from the formation of an effective proton transport pathway. Further, the higher crystalline content and molecular weight of ND when compared to D521 improved the mechanical strength, which was considered to be responsible for enhancing the MEA lifetime by a factor of 6, based on the current density at 0.6 V. This result shows that the improvement in the properties such as the dispersion and crystallinity of ionomers affects the performance and durability of PEFC electrodes without the development of catalysts. Although the development of an electrocatalyst for high activity and durability is important, understanding the ionomer is also very important in that it plays a key role in promoting proton transfer by forming TPB. Further, we would expect the electrode to exhibit a higher level of performance and durability if our ionomer were to be applied with a high-performance catalyst other than the polycrystalline Pt applied in the present study.

MATERIALS AND METHODS

ND fabrication

Nafion 117 film (DuPont Co, NJ, USA) was chosen as the PFSA material for the ND preparation. IPA and H_2SO_4 (purity, 95.0 to 98.0%) were purchased from Aldrich Chemical Co. (USA) and used without additional purification. Before preparing the ND as a cathode binder, Nafion 117 was acidified by treating in 0.5 M boiling H_2SO_4 for 2 hours and in boiling water for another 2 hours (method II) (*37*–*39*). Nafion 117 film in proton form (weight, 12.3 g) was added to a glass liner containing 87.5 g of deionized water and 206.3 g of IPA (volume ratio of 1:3). The glass liner was set up in a high-pressure/high-temperature reactor (4560 Mini-Bench Reactor System, PARR, USA), into which nitrogen was fed until a pressure of 1.5 MPa was reached. The reaction mixture in the reactor was heated to 240°C at a heating rate of 4.25°C min^{-1}. When the pressure reached 11 MPa, the reaction was maintained for 2 hours. The ND was obtained after slowly cooling to atmospheric pressure (101.3 kPa). Last, the ND was filtered using a filter paper with an average pore size of 5 to 10 μm.

Physicochemical analyses of dispersion and solidified ionomer

For the fundamental characterization of the prepared ND and D521 as the reference dispersion, measurements were performed using a DLS system (Zetasizer Nano ZS, Malvern, Worcestershire, UK), viscometer (DV2TLVTJ0, AMETEK Brookfield, MA, USA), and GPC system (EcoSEC GPC system with refractive index and ultraviolet detectors, Tosho Bioscience, PA, USA). Ionomer properties were evaluated in the solid state using XRD (Ultima IV, Rigaku, Tokyo, Japan), SAXS (Beamline 4C SAXS, Pohang, Korea), and field-emission TEM (LIBRA 120, Carl Zeiss, Oberkochen, Germany) analyses.

Fabrication of MEAs

Commercially available 40 wt % Pt/C catalysts (Johnson Matthey, USA) were mixed with deionized water and IPA (Sigma-Aldrich, USA) using a homogenizer (VCX130, Sonics & Materials Inc., USA) for 3 min. Then, 10, 20, and 30 wt % of ND were added to ink slurries and mixed for another 3 min. For the N_2 gas–based catalyst-coated membranes, 3.5 cm × 3.5 cm specimens of Nafion membranes (NR212, DuPont, USA) were pretreated with 1 M H_2SO_4 and 1 M H_2O_2 at 80°C for 1 hour each and then washed. After the pretreatment, the membranes were dried in appropriate frames at room temperature. The prepared ink slurries were sprayed onto the cathode-side membranes. For the anodic MEAs, the aforementioned commercial 40 wt % Pt/C catalyst was prepared using the same method as that used for the cathode, but using D521 (Sigma-Aldrich, USA) instead of the ND. The amount of Pt loading was maintained at 0.2 mg cm^{-2} for all the samples. Surface and cross-sectional images of the MEAs were obtained through field-emission SEM (Merlin COMPACT, Zeiss) at 5 kV in SE mode. Porosity and pore size distributions were obtained via MIP (PM33GT, Quantachrome) after chopping each MEA with the two ionomers applied to less than 25 mm^2.

Electrochemical analysis

The prepared MEAs were assembled with gas diffusion layers (GDL, SGL 35 BC) and Teflon gaskets in the center of each single cell (CNL-PEM005-01, CNL Energy, Korea). Graphite-based serpentine flow fields were applied to both the anode and cathode. The temperatures of the single cells were maintained at 70°C, and the relative humidity was maintained at 100% during the operation of the fuel cell. To activate the MEAs, hydrogen and oxygen were provided to the anode and cathode at a rate of 150 and 200 standard cubic centimeters per minute (sccm), respectively. From the open-circuit voltage, the current was increased at a rate of 50 mA s^{-1} and then held at 5, 10, and 15 A for 10 min. After activation, the MEAs with different ionomers were tested in air; the stoichiometry of H_2 and air was 1.5:4.0 at 2.0 A cm^{-2}. EIS and CV were conducted to measure the resistances and EASs, respectively. CV measurements were conducted under nitrogen at 30°C.

AST for a single cell

To verify the ionomer durability, MEAs with conventional ionomers and the PFSA ND were tested by load cycling after the initial electrochemical analysis. The voltages of the single cells were set to the open-circuit voltage and dropped to 0.35 V as the current density increased (25 mA s^{-1}). After 50 hours of AST, the current-voltage, CV, and EIS values were measured again to determine the effect of the AST. Subsequently, the MEAs were separated from the single cells for TEM characterization. Small amounts of the catalyst layers were collected on lacy carbon grids, and TEM (TECNAI F20, FEI) analysis was conducted at 200 kV.

SUPPLEMENTARY MATERIALS

Supplementary material for this article is available at http://advances.sciencemag.org/cgi/content/full/6/5/eaaw0870/DC1

Fig. S1. Polarization curves for MEAs containing D521 and ND ionomers with different contents.
Fig. S2. Polarization curves and EIS results of MEAs before and after AST in O_2.
Fig. S3. Polarization curves and tabulated results of MEAs with different ionomer loadings before and after AST in air.
Fig. S4. Cyclic voltammograms of MEAs before and after AST.
Fig. S5. TEM images and particle distribution of Pt/C catalysts before and after AST.
Table S1. Current densities at 0.6 V and maximum power densities of MEA-0, MEA-10, MEA-20, and MEA-30 in O_2 and air.
Table S2. Influence of AST on current densities at 0.6 V and maximum power densities of MEA-0 and MEA-20.
Table S3. EIS results for MEA-0 and MEA-20 after AST.

REFERENCES AND NOTES

1. P. Costamagna, S. Srinivasan, Quantum jumps in the PEMFC science and technology from the 1960s to the year 2000: Part I. Fundamental scientific aspects. *J. Power Sources* **102**, 242–252 (2001).
2. G. Sasikumar, J. W. Ihm, H. Ryu, Dependence of optimum Nafion content in catalyst layer on platinum loading. *J. Power Sources* **132**, 11–17 (2004).
3. Z. W. Seh, J. Kibsgaard, C. F. Dickens, I. Chorkendorff, J. K. Nørskov, T. F. Jaramillo, Combining theory and experiment in electrocatalysis: Insights into materials design. *Science* **355**, eaad4998 (2017).
4. I. E. L. Stephens, J. Rossmeisl, I. Chorkendorff, Toward sustainable fuel cells. *Science* **354**, 1378–1379 (2016).
5. M. Watanabe, H. Igarashi, K. Yosioka, An experimental prediction of the preparation condition of Nafion-coated catalyst layers for PEFCs. *Electrochim. Acta* **40**, 329–334 (1995).
6. I. D. Raistrick, Electrode assembly for use in a solid polymer electrolyte fuel cell. U.S. Patent 4876115A (1989).
7. K. D. Kreuer, On the development of proton conducting polymer membranes for hydrogen and methanol fuel cells. *J. Membr. Sci.* **185**, 29–39 (2001).
8. S. J. Hamrock, Membranes and MEAs for dry, hot operating conditions (DOE Hydrogen and Fuel Cell Program, Report No. FY.V.C.1, 662–666, 2011).
9. C. Lei, D. Bessarabov, S. Ye, Z. Xie, S. Holdcroft, T. Navessin, Low equivalent weight short-side-chain perfluorosulfonic acid ionomers in fuel cell cathode catalyst layers. *J. Power Sources* **196**, 6168–6176 (2011).
10. A. Ghielmi, P. Vaccarono, C. Troglia, V. Arcella, Proton exchange membranes based on the short-side-chain perfluorinated ionomer. *J. Power Sources* **145**, 108–115 (2005).
11. C. Welch, A. Labouriau, R. Hjelm, B. Orler, C. Johnston, Y. S. Kim, Nafion in dilute solvent systems: Dispersion or solution? *ACS Macro Lett.* **1**, 1403–1407 (2012).
12. G. Doo, J. H. Lee, S. Yuk, S. Choi, D.-H. Lee, D. W. Lee, H. G. Kim, S. H. Kwon, S. G. Lee, H.-T. Kim, Tuning the ionomer distribution in the fuel cell catalyst layer with scaling the ionomer aggregate size in dispersion. *ACS Appl. Mater. Interfaces* **10**, 17835–17841 (2018).
13. T. T. Ngo, T. L. Yu, H.-L. Lin, Influence of the composition of isopropyl alcohol/water mixture solvents in catalyst ink solutions on proton exchange membrane fuel cell performance. *J. Power Sources* **225**, 293–303 (2013).
14. J. H. Lee, G. Doo, S. H. Kwon, S. Choi, H.-T. Kim, S. G. Lee, Dispersion-solvent control of ionomer aggregation in a polymer electrolyte membrane fuel cell. *Sci. Rep.* **8**, 10739 (2018).
15. S. Holdcroft, Fuel cell catalyst layers: A polymer science perspective. *Chem. Mater.* **26**, 381–393 (2014).
16. Ž. Knez, E. Markočič, M. Leitgeb, M. Primožič, M. Knez Hrnčič, M. Škerget, Industrial applications of supercritical fluids: A review. *Energy* **77**, 235–243 (2014).
17. R. Campardelli, L. Baldino, E. Reverchon, Supercritical fluids applications in nanomedicine. *J. Supercrit. Fluids* **101**, 193–214 (2015).
18. E. Kiran, Supercritical fluids and polymers—The year in review—2014. *J. Supercrit. Fluids* **110**, 126–153 (2016).
19. F. Cansell, C. Aymonier, Design of functional nanostructured materials using supercritical fluids. *J. Supercrit. Fluids* **47**, 508–516 (2009).
20. M. S. Kondratenko, I. V. Elmanovich, M. O. Gallyamov, Polymer materials for electrochemical applications: Processing in supercritical fluids. *J. Supercrit. Fluids* **127**, 229–246 (2017).
21. B. C.-Y. Lu, D. Zhang, W. Sheng, Solubility enhancement in supercritical solvents. *Pure Appl. Chem.* **62**, 2277–2285 (1990).

22. S.-D. Yeo, E. Kiran, Formation of polymer particles with supercritical fluids: A review. *J. Supercrit. Fluids* **34**, 287–308 (2005).
23. P. Girotra, S. K. Singh, K. Nagpal, Supercritical fluid technology: A promising approach in pharmaceutical research. *Pharm. Dev. Technol.* **18**, 22–38 (2013).
24. S. P. Gubin, E. Y. Buslaeva, Supercritical isopropanol as a reducing agent for inorganic oxides. *Russ. J. Phys. Chem. B* **3**, 1172–1186 (2009).
25. A. Thaler, K. Hintzer, K. H. Lochhaas, F. Maerz, S. J. Hamrock, Aqueous emulsion polymerization of functionalized fluoromonomers. U.S. Patent 20050096442 (2006).
26. C. D. Peter, Process for homopolymerization of tetrafluoroethylene and copolymerization of same with fluoro co-monomers in the solvent 1,1,2-trichloro-1,2,2-trifluoroethane. U.S. Patent 3528954A (1970).
27. E. K. Yu, S. A. Smirnov, M. P. Yu, F. T. Sergei, Perfluorinated carbon-chain copolymers with functional groups and cation exchange membranes based on them: Synthesis, structure and properties. *Russ. Chem. Rev.* **59**, 560 (1990).
28. F. L. Harry Allcock, James E. Mark, *Contemporary Polymer Chemistry* (Prentice Hall, ed. 2, 1990).
29. T. E. Attwood, P. C. Dawson, J. L. Freeman, L. R. J. Hoy, J. B. Rose, P. A. Staniland, Synthesis and properties of polyaryletherketones. *Polymer* **22**, 1096–1103 (1981).
30. M. T. Bishop, F. E. Karasz, P. S. Russo, K. H. Langley, Solubility and properties of a poly(aryl ether ketone) in strong acids. *Macromolecules* **18**, 86–93 (1985).
31. E. Passalacqua, F. Lufrano, G. Squadrito, A. Patti, L. Giorgi, Nafion content in the catalyst layer of polymer electrolyte fuel cells: Effects on structure and performance. *Electrochim. Acta* **46**, 799–805 (2001).
32. J. W. Lim, Y.-H. Cho, M. Ahn, D. Y. Chung, Y.-H. Cho, N. Jung, Y. S. Kang, O.-H. Kim, M. J. Lee, M. Kim, Y.-E. Sung, Ionic resistance of a cathode catalyst layer with various thicknesses by electrochemical impedance spectroscopy for PEMFC. *J. Electrochem. Soc.* **159**, B378–B384 (2012).
33. J. M. Song, S. Y. Cha, W. M. Lee, Optimal composition of polymer electrolyte fuel cell electrodes determined by the AC impedance method. *J. Power Sources* **94**, 78–84 (2001).
34. C.-M. Lai, J.-C. Lin, F.-P. Ting, S.-D. Chyou, K.-L. Hsueh, Contribution of Nafion loading to the activity of catalysts and the performance of PEMFC. *Int. J. Hydrogen Energy* **33**, 4132–4137 (2008).
35. J. Xie, F. Xu, D. L. Wood III, K. L. More, T. A. Zawodzinski, W. H. Smith, Influence of ionomer content on the structure and performance of PEFC membrane electrode assemblies. *Electrochim. Acta* **55**, 7404–7412 (2010).
36. Y.-H. Cho, S. J. Yoo, I.-S. Park, T.-Y. Jeon, Y.-H. Cho, J. W. Lim, O. J. Kwon, W.-S. Yoon, Y.-E. Sung, Characteristics and performance of membrane electrode assemblies with operating conditions in polymer electrolyte membrane fuel cell. *Electrochim. Acta* **56**, 717–721 (2010).
37. F. Wang, M. Hickner, Y. S. Kim, T. A. Zawodzinski, J. E. McGrath, Direct polymerization of sulfonated poly(arylene ether sulfone) random (statistical) copolymers: Candidates for new proton exchange membranes. *J. Membr. Sci.* **197**, 231–242 (2002).
38. M. J. Sumner, W. L. Harrison, R. M. Weyers, Y. S. Kim, J. E. McGrath, J. S. Riffle, A. Brink, M. H. Brink, Novel proton conducting sulfonated poly(arylene ether) copolymers containing aromatic nitriles. *J. Membr. Sci.* **239**, 199–211 (2004).
39. Y. Li, F. Wang, J. Yang, D. Liu, A. Roy, S. Case, J. Lesko, J. E. McGrath, Synthesis and characterization of controlled molecular weight disulfonated poly(arylene ether sulfone) copolymers and their applications to proton exchange membranes. *Polymer* **47**, 4210–4217 (2006).

Acknowledgments: We thank our colleagues for their contributions to this work. **Funding:** This work was supported by Project Code IBS-R006-A2 and the Korea Institute of Energy Technology Evaluation and Planning (KETEP) and the Ministry of Trade, Industry & Energy (MOTIE) of the Republic of Korea (No. 20183010032380). This work was also supported by the Technology Development Program to Solve Climate Changes of the National Research Foundation (NRF) funded by the Ministry of Science and ICT (grant NRF-2018M1A2A2063172). This research was also supported by Korea Electric Power Corporation (grant number R16VA08). **Author contributions:** C.-Y.A. analyzed the data and electrochemical experiments and wrote the manuscript in collaboration with C.H.L. Y.-H.C. conceived the idea and designed the experiments. J.A. synthesized and characterized the ND with assistance from D.W.L. and J.H.L. J.G.S. and Y.-H.C. constructed the experimental apparatus for the fuel cell tests and performed those tests. In addition, C.H.L. contributed to the planning and coordination of the project. Y.-H.C. and Y.-E.S. coordinated and supervised the entire project. C.-Y.A., S.Y.K., O.-H.K., Y.-H.C., and C.H.L. discussed the results. All authors commented on the manuscript. **Competing interests:** The authors declare that they have no competing interests. **Data and materials availability:** All data needed to evaluate the conclusions in the paper are present in the paper and/or the Supplementary Materials. Additional data related to this paper may be requested from the authors.

Submitted 16 November 2018
Accepted 21 November 2019
Published 31 January 2020
10.1126/sciadv.aaw0870

Citation: C.-Y. Ahn, J. Ahn, S. Y. Kang, O.-H. Kim, D. W. Lee, J. H. Lee, J. G. Shim, C. H. Lee, Y.-H. Cho, Y.-E. Sung, Enhancement of service life of polymer electrolyte fuel cells through application of nanodispersed ionomer. *Sci. Adv.* **6**, eaaw0870 (2020).

Enhancement of service life of polymer electrolyte fuel cells through application of nanodispersed ionomer

Chi-Yeong Ahn, Juhee Ahn, Sun Young Kang, Ok-Hee Kim, Dong Woog Lee, Ji Hyun Lee, Jae Goo Shim, Chang Hyun Lee, Yong-Hun Cho and Yung-Eun Sung

Sci Adv **6** (5), eaaw0870.
DOI: 10.1126/sciadv.aaw0870